4π studies of the 1.8–4.8 GeV ^{3}He+ ^{nat}Ag, ^{197}Au reactions. I. Energy deposition

K. B. Morley, K. Kwiatkowski, D. S. Bracken, E. Renshaw Foxford, V. E. Viola, L. W. Woo,* and N. R. Yoder
Departments of Chemistry and Physics and Indiana University Cyclotron Facility, Indiana University, Bloomington, Indiana 47405

R. Legrain, E. C. Pollacco, and C. Volant
Commissariat à l'Energie Atomique, DAPNIA Service de Physique Nucléaire, C.E. Saclay, 91191 Gir-sur-Yvette Cedex, France

R. G. Korteling
Department of Chemistry, Simon Fraser University, Burnaby, British Columbia, Canada

H. Breuer
University of Maryland, College Park, Maryland 20742

J. Brzychczyk
Institute of Physics, Jagiellonian University, 30-059 Krakow, Poland
(Received 11 December 1995)

The Indiana Silicon Sphere 4π detector has been used to measure light-charged particles and intermediate-mass fragments (IMFs) emitted in the 18–4.8 GeV ^{3}He+ ^{nat}Ag, ^{197}Au reactions. Ejectile multiplicity and total event kinetic energy distributions scale systematically with projectile energy and target mass, except for the ^{nat}Ag target at 3.6 and 4.8 GeV. For this system, a saturation in deposition energy is indicated by the data, suggesting the upper projectile energy for stopping has been reached. Maximum deposition energies of ~950 MeV for the ^{nat}Ag target and ~1600 MeV for the ^{197}Au target are inferred from the data. The results also demonstrate the importance of accounting for fast cascade processes in defining the excitation energy of the targetlike residue. Correlations between various observables and the average IMF multiplicity indicate that the total thermal energy and total observed charge provide useful gauges of the excitation energy of the fragmenting system. Comparison of the experimental distributions with intranuclear cascade predictions shows qualitative agreement. [S0556-2813(96)06108-0]

PACS number(s): 21.65.+f, 25.55.−e, 25.70.Lm

I. INTRODUCTION

In order to investigate the behavior of nuclear matter under extreme conditions of temperature, target-projectile interactions that deposit excitation energies up to and beyond the total nuclear binding energy are required. For light-ion-induced reactions, this situation can be achieved via hard nucleon-nucleon scatterings and the excitation of Δ and higher resonances in central collisions, followed by rescattering and/or reabsorption of the decay pions in medium [1–7]. Nuclei excited in this way are unique in that a high energy-density region can be created in the nuclear interior on a time scale that is short ($\lesssim$30 fm/c) with respect to the time for evolution of the nuclear mean field [2,5,8–10]. Subsequent destabilization of the system occurs primarily by thermal processes—in contrast to heavy-ion-induced reactions, where compressional and rotational effects influence the breakup dynamics strongly. Thus, light-ion and heavy-ion studies complement one another in attempts to understand the nuclear equation of state, each following distinctly different paths toward disassembly as they evolve in the nuclear temperature-density phase diagram [11,12].

A critical aspect of efforts to study the nuclear equation of state involves experimental determination of the thermal properties and subsequent decay modes of hot residues formed in energetic central collisions. For light-ion-induced reactions this is especially important due to the broad distribution of deposition energies and residue masses formed during the fast cascade in the early stages of the collision [2–7]. Thus, it is essential to identify experimental observables that aid our understanding of the reaction dynamics and can be subsequently related to the energy deposition process. This is also necessary to test the predictions of various transport models [2,3,7–10]—which serve as input for hybrid calculations designed to describe the decay dynamics of hot nuclear systems (see, for example, Refs. [4,13]).

Experimental attempts to test transport-model predictions for light-ion-induced reactions in the bombarding energy regime up to ~10 GeV/nucleon have focused for the most part on hadron spectra [2,3,7]. While such studies have demonstrated the relative success of the current codes, these spectra relate more directly to the dissipation of energy by the projectile in the nuclear medium, rather than the question of deposition energy in the hot residue. Due to the rapid time evolution of collisions above several hundred MeV/per nucleon, definition of these quantities is not straightforward. This is especially true for central collisions, which demand an understanding of energy evolution in the interaction zone, including hadronization, dissipation time scales, and in-medium rescattering and reabsorption effects. The problem of pion reabsorption is a central issue, since this process

*Sabbagh Associates, Bloomington, IN 47402.

 © 1996 The American Physical Society

plays an important role in the rapid conversion of relative projectile energy into internal excitation energy of the residue [2,4].

Early studies of energy deposition in energetic light-ion-induced reactions demonstrated a significant probability for the formation of highly excited residual nuclei [14–16]. In addition, linear momentum transfer studies [17–19] showed that the deposition energy is a broad continuum. However, in order to evaluate the deposition energy more qualitatively, it is essential to perform more exclusive studies of the residue breakup dynamics. Recently, Pienkowski *et al.* [20] have measured neutron multiplicities in 2.0 GeV proton- and ^{3}He-induced reactions on several targets. Their results are in approximate accord with intranuclear cascade predictions and indicate residue excitation energies up to $E^*/A \approx 5$ MeV/residue nucleon. Further, emulsion studies have suggested a saturation in the deposition energy at somewhat higher values of E^*/A [7].

This paper and that which follows [21] present results from the first measurements of GeV light-ion-induced reactions in which both light-charged particles (LCP=H and He isotopes) and intermediate-mass fragments (IMF: $3 \leqslant Z \lesssim 20$) are fully Z identified with very low energy thresholds and large solid-angle coverage. The reactions of 1.8, 3.6, and 4.8 GeV ^{3}He ions with ^{nat}Ag and 1.8 and 4.8 HeV ^{3}He with ^{197}Au were studied using the Saturne II accelerator at the Laboratoire National Saturne (E228). Detection of LCP's and IMF's was performed with the Indiana Silicon Sphere 4π detector array (ISiS). The intent of these first two papers is to survey the results as they pertain questions of (1) reaction dynamics and deposition energy [22] and (2) multifragmentation and the nuclear equation of state [23]. Subsequent investigations will examine specific aspects of these results.

The goal of this paper is to investigate several experimental variables that reflect the collision violence, and more specifically, the question of deposition energy in the hot residues. We first describe the experimental measurements and then examine the experimental distributions of several variables commonly associated with collision violence and deposition energy, as well as the correlations among these. Comparisons are also made with the predictions of an intranuclear cascade (INC) calculation [3], followed by a summary of conclusions.

II. EXPERIMENTAL MEASUREMENT

A. The Indiana silicon sphere 4π detector array

The ISiS array, described in detail elsewhere [24], is based on a spherical geometry and is designed primarily for the study of light-ion-induced reactions. It consists of 162 triple detector telescopes—90 in the forward hemisphere and 72 in the backward hemisphere—covering the polar angular ranges from 14° to 86.5° and 93.5° to 166°. The design consists of eight rings, each composed of 18 truncated-pyramid telescope housings. To increase granularity at angles near 0°, the forwardmost ring is segmented into two components. A sketch of the detector configuration in the forward hemisphere is shown in Fig. 1.

Each telescope is composed of (1) a gas-ionization chamber (GIC) operated at 16–18 Torr of C_3F_8 gas; (2) a fully depleted 500 μm ion-implanted passivated silicon detector, Si(IP), and (3) a 28 mm thick CsI(Tl) crystal with light guide and photodiode readout. The CsI elements were also used as hit detectors that provided multiplicity information on minimum ionizing particles. Detectors are operated in a common gas volume; vacuum isolation is provided by a graphite-coated, 250 μg/cm^2 polypropylene window supported by an aluminum cagelike structure, matched to the geometry of the telescope housings and the passivated detector edges. The window also served as a cathode for the ion chambers. The telescope dynamic range permitted measurement of LCP's and IMF's up to $Z \approx 20$ with discrete charge resolution over the dynamic range $0.8 \leqslant E/A \leqslant 96$ MeV. The low energy threshold for Z identification includes the effects of target and window thicknesses, as well as the pressure in the gas-ionization chamber and the silicon surface dead layer. The Si(IP)/CsI(Tl) telescopes also provide particle identification (Z and A) for energetic H, He, Li, and Be isotopes ($E/A \geqslant 8$ MeV). The Si(IP) detectors constitute a critical component of the array, providing both excellent energy resolution and facilitating reliable energy calibrations for the GIC and CsI(Tl) elements.

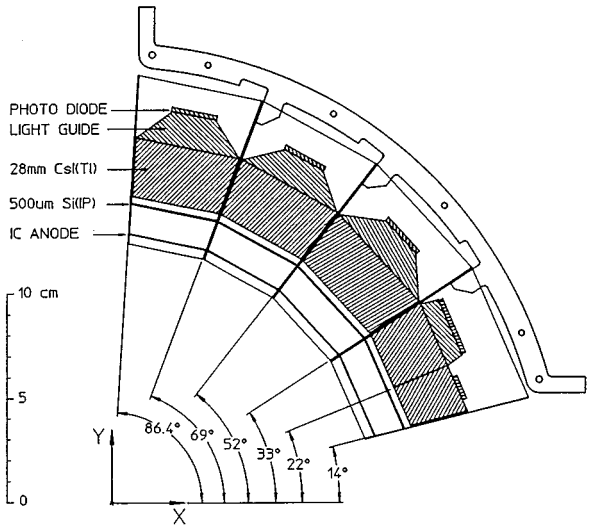

FIG. 1. Configuration for one arc of detector telescopes in forward hemisphere for Indiana Silicon Sphere [24]. Four annular segments containing eighteen such arcs fit together to cover one hemisphere from 14° to 86.5° in polar angle. At the smallest angles, each detector module is divided into two halves to increase granularity. The x axis coincides with the beam direction.

B. Experimental details

Two types of targets were utilized in the experiments: 35×35 mm^2 foil targets mounted directly on 5 mm^2 target frames and 6×6 mm^2 foil targets supported at the sides by two 10 μm-diameter carbon fibers stretched vertically across the frame [25]. The experiments on ^{197}Au used a 6×6 mm^2 target thickness 1.53 mg/cm^2. The experiments on ^{nat}Ag utilized both a 6×6 mm^2 target of thickness 1.08 mg/cm^2 and a 35×35 mm^2 foil of the same thickness. For most of the data acquisition, the smaller-area targets were used to ensure that detected events originated from interactions near the center of the detector array. The larger-area

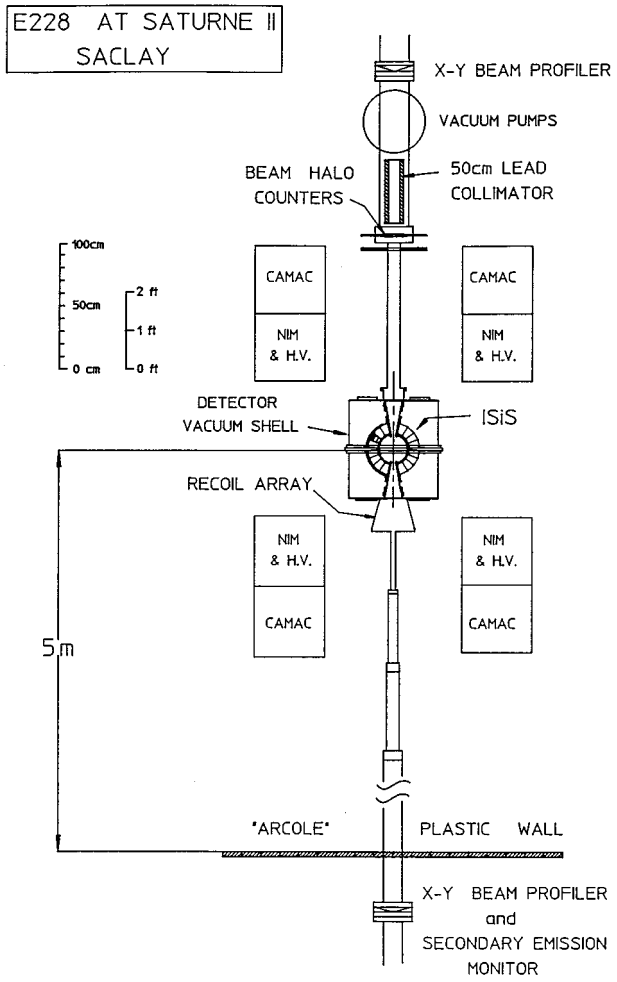

FIG. 2. Experimental layout at the Saturne II accelerator for experiment E228. Detector elements include the ISiS array, the recoil array, and the forward plastic wall (ARCOLE). Equipment related to the beam quality includes two *x-y* position-sensitive profilers, a 50 cm long lead collimator, beam halo counters (active collimators), and a secondary emission monitor.

targets were used to estimate the percentage of beam that missed the smaller targets, providing a basis for calculating absolute cross sections. A blank target was regularly placed in the target position to evaluate any contributions from beam halo striking the target frame; these were found to be negligible in all cases.

Beam intensities ranged from $0.5–1.1\times10^8$ particles/spill. The beam spill length was approximately 500 ms and the repetition cycle was 1.20, 2.56, and 4.01 s at beam energies of 1.8, 3.6, and 4.8 GeV, respectively. The relative beam intensity was monitored throughout the experiments by a secondary-emission monitor placed in front of the beam dump.

The experimental layout is illustrated in Fig. 2. Two *x-y* position-sensitive beam profilers, one upstream and one downstream of ISiS, provided information for beam tuning. The secondary emission monitor was located just downstream of the second profiler. A 50 cm long lead collimator (inner diameter=9 cm, outer diameter=18 cm), located 1.3 m upstream of the target, was inserted to protect those silicon detectors nearest the beam axis from radiation damage during beam tuning. In addition, an active-collimator system consisting of eight fast-plastic scintillator segments was located directly downstream of the lead collimator at the entrance of ISiS. An inner active collimator was located inside the beam pipe and consisted of four, 2 cm thick paddles shaped to form four quadrants of a disk with an inner diameter of 3 cm and an outer diameter of 16 cm. Four outer active collimators were arranged to surround the outside of the beam pipe and consisted of 50×20 cm^2 paddles of thickness approximately 0.6 cm. This combined system shadowed the entire active cross sectional area of ISiS relative to the beam axis.

For the data presented here, a multiplicity of two in the silicon fast logic was set as a minimum-bias trigger. The signal conditioning, trigger logic, and data acquisition for ISiS are described in more detail in Ref. [24]. A recoil array attached to the downstream end of ISiS was designed to detect heavy recoil nuclei and a fast-plastic wall (ARCOLE) was located 5 m downstream to detect fast leading particles. Results from these components of the experiment will be discussed in subsequent publications. In addition, analog-to-digital converter (ADC) hit registers for all CsI(Tl) detectors were checked whenever an ISiS event occurred. If a CsI(Tl) detector registered an event above a fixed threshold energy ($\sim$20 MeV), but with no corresponding silicon detector signal, then the CsI(Tl) ADC channel was read and included in the event buffer. These signals are referred to as minimum-ionizing particles (MIPs) and correspond to energetic particles (primary hydrogen isotopes) with energy loss too low in the silicon detector to produce a trigger signal that exceeded the fast-timing threshold.

C. Data analysis

One of the major features of the ISiS array is the excellent energy resolution provided by the silicon elements in each telescope. Linearity of the silicon detectors was calibrated with a CAMAC computer-controlled pulser system [26]; a linear equation was fit to the pulser centroids for each channel. Absolute calibrations were obtained using a charge-terminated ORTEC 448 precision pulse generator, calibrated with a ^{241}Am source. The calibrations were found to be consistent to about 1.5% with LCP punch-through energies. Ionization-chamber calibrations were made relative to a ^{241}Am source, with and without C_3F_8 gas in the ISiS array. In addition, points of different ^{4}He energy in the calibrated silicon detector were employed along with energy-loss tables for ^{4}He in C_3F_8 [27] in the calibration procedure. The absolute errors in the ionization-chamber calibrations are about $\pm5\%$. All ionization chamber and silicon calibrations included energy-loss corrections for target thickness, window thickness, and silicon dead layers.

The CsI(Tl) crystals were calibrated in a similar manner to the ionization chambers. Each calibrated-silicon energy signal was plotted versus its corresponding uncalibrated photodiode signal. An energy loss program [28] was used to obtain the CsI energy from the known energy loss in the silicon detector and a linear equation was fit to the CsI/(Tl) energy versus channel number. Because the calibrations for all isotopes of a given element were similar, the calibration values for a given telescope and charge were averaged to-

TABLE I. The number of valid trigger events (multiplicity $\geqslant 2$) after data have been filtered through the gating conditions.

System	Total events	Events with at least one IMF
1.8 GeV ^{3}He+^{nat}Ag	5 405 691	822 993
3.6 GeV ^{3}He+^{nat}Ag	6 301 388	1 606 407
4.8 GeV ^{3}He+^{nat}Ag	4 636 509	1 276 631
1.8 GeV ^{3}He+^{197}Ag	1 178 124	267 543
4.8 GeV ^{3}He+^{197}Ag	3 928 244	1 639 313

gether to facilitate the data replay. Individual LCP (p,d,t, ^{3}He, ^{4}He, and Li) gates were set for each silicon/photodiode pair.

Events which fired in coincidence with high energy light-charged particles in the active collimators (about 10% of the events) were eliminated from the analysis in replay. A gate was also set to eliminate data corresponding to the first 40–70 ms of the beam spill. The number of valid trigger events (charged-particle multiplicity $\geqslant 2$) for each system and the number of valid trigger events in which at least one IMF was detected are tabulated in Table I.

III. EXPERIMENTAL RESULTS

The distribution of excitation energies deposited in the residual nuclei during the initial cascade has been examined via several experimental variables believed to be related to deposition energy (see, for example, Ref. [29]). These include observed multiplicity distributions for LCP's ($N_{\rm LCP}$), IMF's ($N_{\rm IMF}$), and total charged particles ($N_{\rm tot}$); total observed charge ($Z_{\rm obs}$), and total observed transverse and thermal energy ($E_\perp$ and $E_{\rm th}$, defined later). Results are presented in terms of relative probability distributions, with $\Sigma_i N_i/N=1$. Self-consistent comparison among the five data sets was assured by removing from the analysis any telescope that was not continuously functional throughout the experiment. This resulted in an identical detector acceptance of 67% of 4π obtained in the ^{3}He+^{nat}Ag reaction and 69% for the ^{4}He+^{197}Au reaction.

A. Multiplicity and energy distributions

One important gauge of deposition energy is the number of IMF's emitted in a given event. IMF multiplicity is predicted to be strongly correlated with excitation energy [30–32], at least until the internal energy of the system approaches the vaporization limit. In Fig. 3, the observed IMF multiplicity distributions for the 1.8–4.8 GeV ^{3}He+^{nat}Ag, ^{197}Au systems are shown. As a general trend, the maximum observed IMF multiplicity scales with projectile energy. However, the IMF multiplicity distributions for the 3.6 and 4.8 GeV ^{3}He+^{nat}Ag reactions are nearly identical, suggesting that deposition energy may be similar for these two projectile energies.

Comparison of the results for the two targets at 4.8 GeV bombarding energy shows a distinctly higher maximum multiplicity for ^{197}Au ($M_{\rm IMF}^{\rm max}\sim 10$) relative to ^{nat}Ag($M_{\rm IMF}^{\rm max}\sim 7$) at the 10^{-6} relative probability level. This is roughly in proportion to the upper limits of excitation energy predicted for

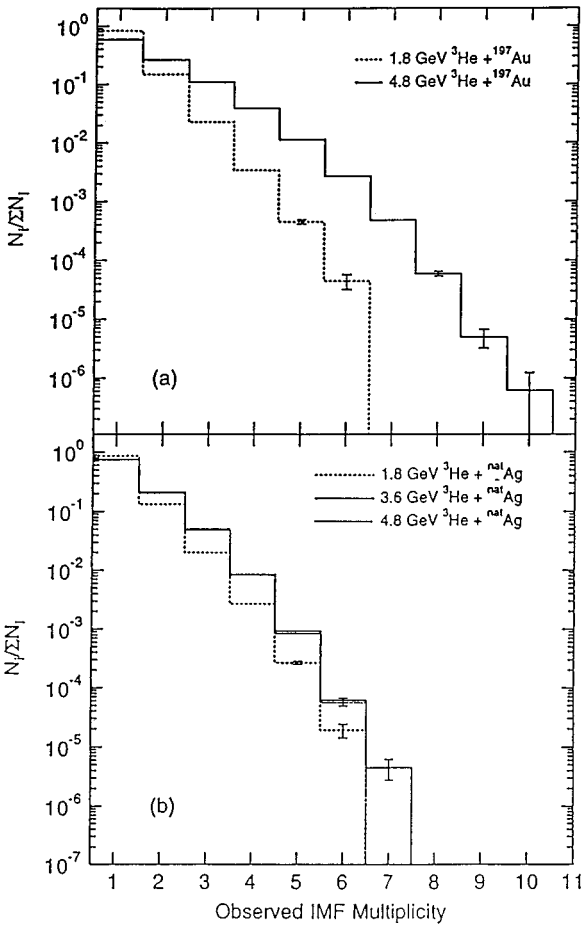

FIG. 3. Measured IMF multiplicity distributions for (top) the 1.8 and 4.8 GeV ^{3}He+^{197}Au reactions and (bottom) 1.8, 3.6, and 4.8 GeV ^{3}He+^{nat}Ag reactions. Error bars are statistical only. Distributions are not corrected for detector geometric efficiency.

these two systems by intranuclear cascade calculations [3]: ($\sim$1500 MeV for ^{197}Au and $\sim$1000 MeV for ^{nat}Ag). However, the larger mass of the ^{197}Au target also influences this result. Finally, the 1.8 GeV ^{3}He+^{nat}Ag system, which is predicted to have the lowest average excitation energy, exhibits the lowest average multiplicity, although the ^{197}Au system at 1.8 GeV is not significantly higher, due in part to the proximity of this system to the multifragmentation threshold [30–32]. We note here that the IMF multiplicity distribution measured in this work for 4.8 GeV ^{3}He+^{197}Au differs distinctly from that reported in Ref. [33] for the similar 4.0 GeV ^{4}He+^{197}Au system. This is discussed in more detail in Ref. [21].

The IMF multiplicities provide a rather coarse gauge of the excitation energy distributions due to the relatively small number of fragments. As an alternative, we examine two observables commonly used in heavy-ion reaction studies [16,29,34,35], the multiplicities of light-charged particles ($N_{\rm LCP}$) and total charged particles ($N_{\rm tot}=N_{\rm LCP}+N_{\rm IMF}$). These are shown in Fig. 4 and are similar in character to those for IMF's. One distinct difference between the LCP/total charged particle distributions and those for IMF's is found in the 3.6 and 4.8 GeV ^{3}He+^{nat}Ag systems, where the higher projectile energy leads to higher maximum multiplici-

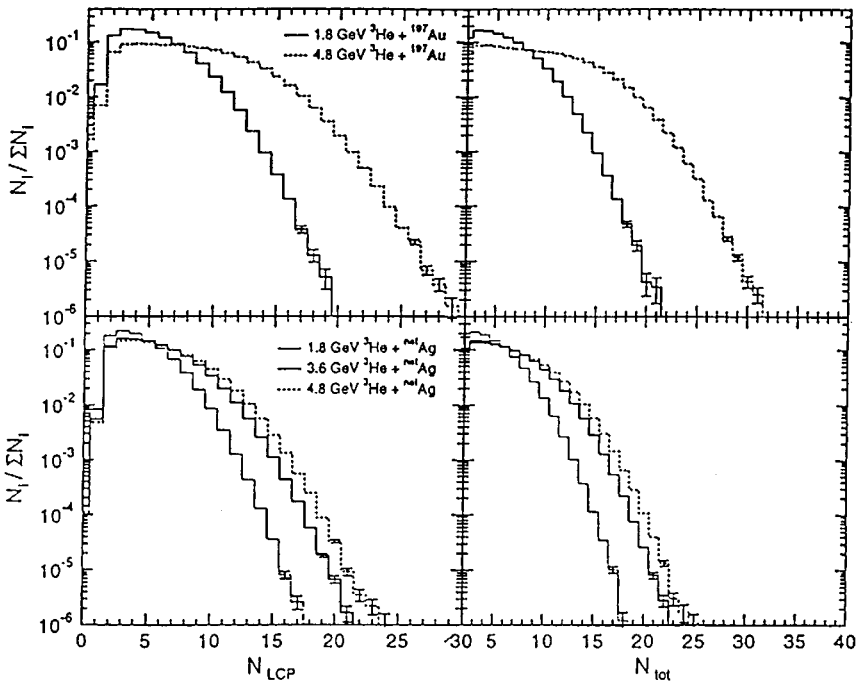

FIG. 4. Measured LCP and total charged-particle multiplicity distributions for the 1.8 and 4.8 GeV ^{3}He+^{197}Au reactions (top) and 1.8, 3.6, and 4.8 GeV ^{3}He+^{nat}Ag reactions (bottom). Error bars are statistical only.

ties. However, the LCP distribution includes a significant contribution from ejectiles emitted during the fast cascade/nonequilibrium stages of the reaction. These latter contributions are illustrated in Fig. 5, which shows relative differential cross sections for the fragment kinetic energy distributions gated on $M_{\mathrm{IMF}}=2$ for He, Li, and C fragments emitted at 14°–22° in the 4.8 GeV ^{3}He+^{nat}Ag reaction. The significant yields of energetic ejectiles are apparent and demonstrate that even for the more violent events, nonequilibrium processes compose an important fraction of the yield. These observations suggest that the LCP distributions of Fig. 4 may serve as a better gauge of the energy dissipated by the projectile than the actual deposition energy in the hot residual nucleus. Also shown in Fig. 5 are two-component moving-source fits [21,36,37] to the Li and C data (solid lines). The dashed lines give the equilibriumlike fit component and the difference represents nonequilibrium processes.

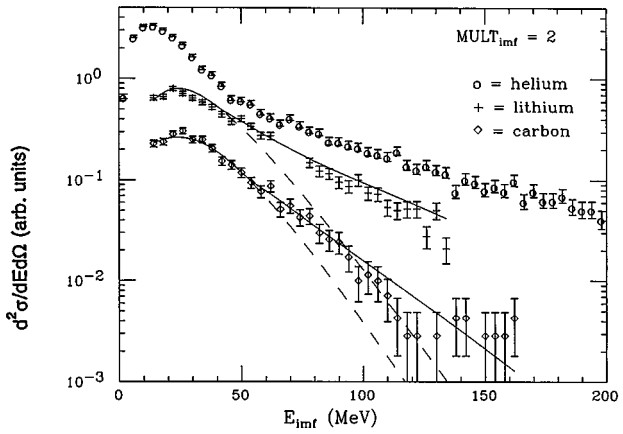

FIG. 5. Spectra of He, Li, and C fragments for $M_{\mathrm{IMF}}=2$ events at 14°–22°. Data are from 4.8 GeV ^{3}He+^{nat}Ag system. Solid lines are two-component moving-source fits to the Li and C spectra; dashed lines represent the corresponding slow component.

To investigate the effect of nonequilibrium emission, we have schematically separated all ejectile spectra into thermal and fast components. The division takes advantage of the excellent energy definition provided by the silicon elements in the ISiS array, combined with minimal source kinematic effects in these reactions—which provide nearly complete, high quality spectra for all fragments over the full angular range. The separation procedure is based on analysis of the systematic behavior of the Maxwellian-like spectra and the distinct slope change in the exponential tails of the LCP and IMF inclusive spectra (especially prominent for $Z=2$ fragments in Fig. 5). For each Z value, thermal charged particles (N_{th}) are defined to be those ejectiles with energies (ϵ^i_{th}) below a cutoff energy

$$\epsilon^{\max}_{\mathrm{th}} = C_0 Z_f + \epsilon_0 . \tag{1}$$

This cutoff energy corresponds approximately to the region where the slope of the spectral tail changes, most evident for He ions in Fig. 5. In Eq. (1), Z_f is the fragment charge, C_0 is a spectral peak parameter determined from fits to the most probable peak energies, and $\epsilon_0=31$ MeV is a constant based upon the two-component moving-source fits illustrated in Fig. 5. The parameter C_0 is weakly dependent on both target mass and beam energy. Values of ϵ^i are evaluated in the source reference frame, as determined from both rapidity and moving-source fits to the spectra [21,36,37]. Fragments with energies above this $\epsilon^{\max}$ cutoff energy are labeled fast (N_{fast}), and are important primarily for $Z=1$–4 ejectiles. The extracted observables show little sensitivity to the division point over a ± 10 MeV interval in ϵ_0.

The results of this analysis are shown in Fig. 6, where distributions for N_{th} and N_{fast} are plotted. For the Ag target, the multiplicity distributions for thermal events are nearly the same at 3.6 and 4.8 GeV. However, the fast particles are clearly enhanced at the higher bombarding energy, suggesting less stopping and more intense spray of fast ejectiles.

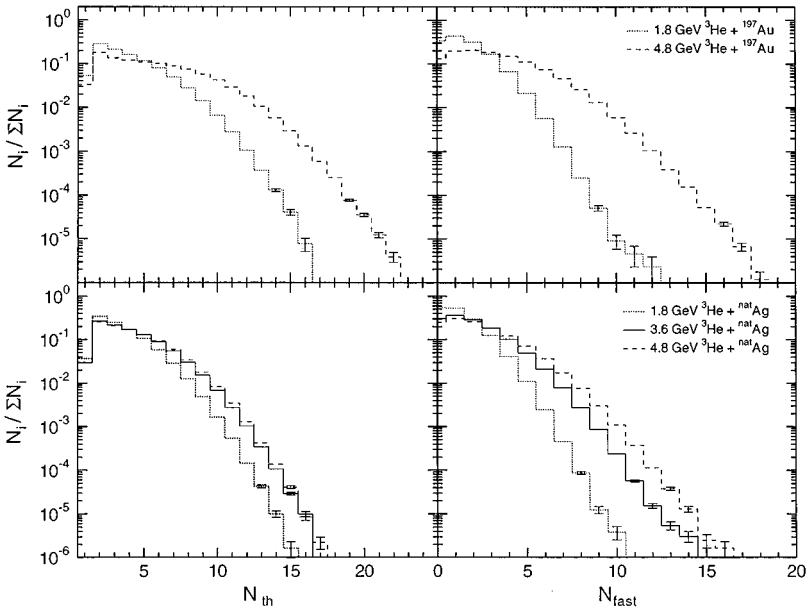

FIG. 6. Comparison of thermal (left) and fast (right) multiplicity distributions for the ^{3}He+ ^{nat}Ag and ^{197}Au systems, as described in text. Systems are defined on figure.

This analysis emphasizes the need to eliminate fast cascade/nonequilibrium events whenever particle multiplicity or fragment charge/isotope distributions are used as an indicator of excitation energy.

Another observable that provides a continuous distribution is the total energy of all fragments emitted in an event, $E_{\rm tot}$, which, in principle, should be related to the excitation energy of the emitting source. In Fig. 7, we show the distributions for the systems studied here. At the 10^{-5} probability level, event energies are observed up to $E_{\rm tot}\sim 900$ MeV for Ag and $E_{\rm tot}\sim 1200$ MeV for ^{197}Au at the highest bombarding energy. However, as is evident from the spectra in Fig. 5, a significant fraction of $E_{\rm tot}$ may originate in fast cascade/nonequilibrium events that are not representative of the excitation energy of the fragmentating source.

In order to define an observable that is more directly related to the excitation energy of the multifragmenting system and minimizes preequilibrium contributions, we have constructed a sum of the kinetic energies for all thermal ejectiles in an event. This quantity is defined as the total thermalized energy

$$E_{\rm th}=\Sigma\,\epsilon^{i}_{\rm th}. \qquad (2)$$

This definition does not necessarily imply full statistical equilibrium, but rather is an indicator of the internal energy available to drive the disassembly process.

The $E_{\rm th}$ distributions shown in Fig. 8 scale systematically with projectile energy and target mass, analogous to the behavior of the IMF and thermal ejectile multiplicity distributions. The 3.6 and 4.8 GeV $E_{\rm th}$ distributions are also nearly identical for the ^{3}He+Ag system. The similarity of the IMF, $N_{\rm th}$, and $E_{\rm th}$ distributions suggest that the deposition energy saturates near 4 GeV for the Ag target. Similar saturation effects have previously been proposed from interpretation of 3–5 GeV proton interactions with emulsions [7]. Many effects contribute to the saturation of deposition energy in this energy range, including (1) the leveling of the total *N*-*N* cross section; (2) increasingly forward-peaked *N*-*N* elastic and inelastic angular distributions; (3) the increase in the secondary pion momenta above the (3,3) resonance, which decreases the probability of Δ excitations, and (4) as pointed out in Refs. [5] and [7], the depletion of the nucleon density in the central collision region. The net result is a saturation and/or decrease in the transverse *N*-*N* momentum transfer [38], which produces an increasingly forward-focused flow

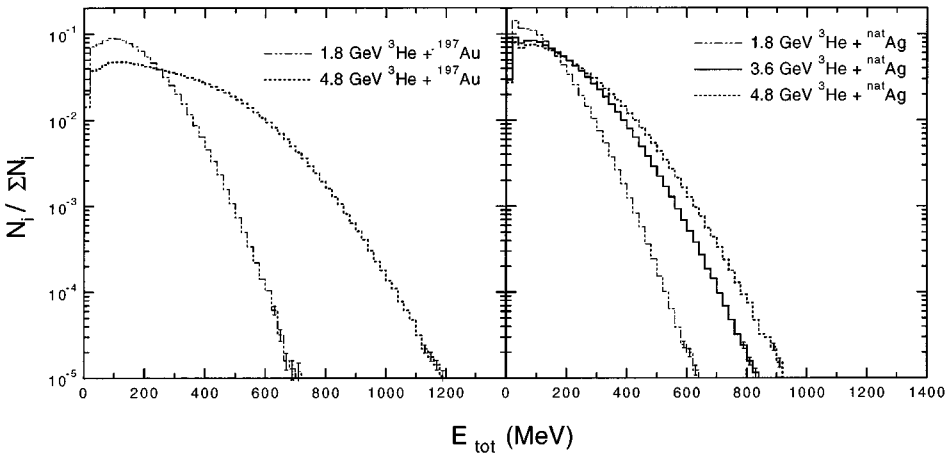

FIG. 7. Total emitted energy per event for ^{3}He+ ^{197}Au system (left frame) and ^{3}He+ ^{nat}Ag (right frame).

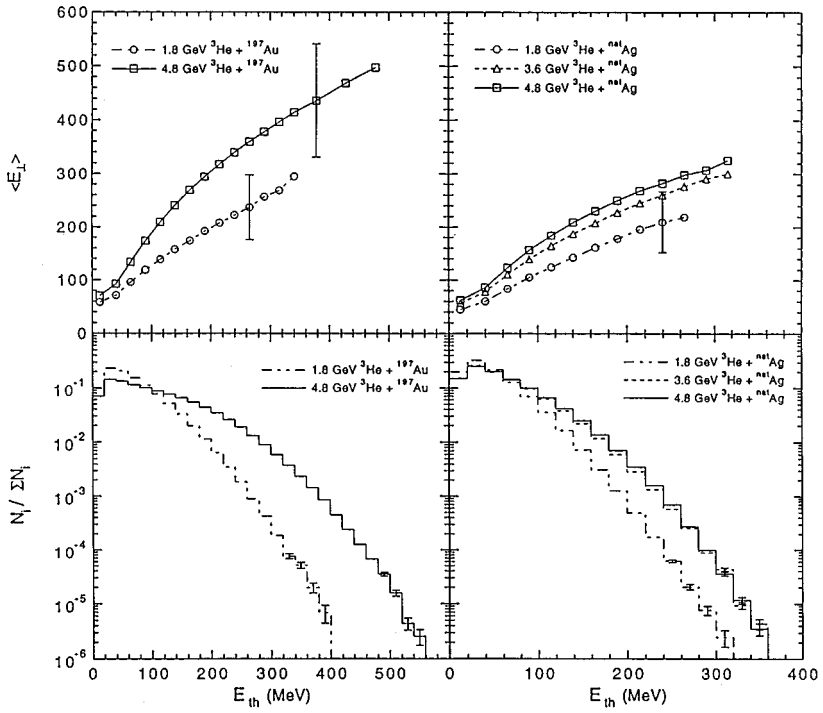

FIG. 8. Lower frames: distributions of observed total thermalized energy per event for ^{3}He+^{197}Au (left) and ^{3}He+^{nat}Ag (right); upper frames: correlation between total thermalized energy and transverse energy. Error bars indicate standard deviations of distribution widths ($\pm\sigma$) and are representative of data. Systems are defined on figure.

of energy with increasing projectile energy beyond a few GeV.

Also shown in Fig. 8 is the correlation between $E_{\rm th}$ and the total observed transverse energy per event, $E_\perp = \Sigma_i E_i \sin^2\theta$. The error bars represent the full width at half maximum of the distributions. In calculating $E_\perp$, no distinction is made between thermal and fast ejectiles, consistent with the use of this variable in heavy-ion studies. There is good scaling between $E_{\rm th}$ and $E_\perp$ at the highest thermal energies. However, this agreement is in part due to the cumulative sum of small nonequilibrium components in the calculation of $E_\perp$, which exert a nonnegligible influence on its magnitude. As $E_{\rm th}$ decreases, $E_\perp$ systematically deviates above $E_{\rm th}$, presumably due to the more peripheral origin of these events. For the ^{3}He+^{nat}Ag system, $E_\perp$ is systematically $\sim$10% higher at 4.8 GeV than at 3.6 GeV, consistent with the results for the total energy shown in Fig. 7. This suggests that $E_\perp$ may serve as a better gauge of the energy dissipated by the projectile, whereas $E_{\rm th}$ relates more directly to the energy deposited in the heavy residual nucleus.

At the 10^{-6} probability level, the maximum observed values of $E_{\rm th}\sim$350 MeV for the ^{nat}Ag residue and $\sim$550 MeV for ^{197}Au indicate the attainment of significant deposition energies in these reactions. These values translate into maximum deposition energies of the order of 950 MeV for the ^{nat}Ag residue and 1600 MeV for the ^{197}Au residue, after first-order corrections are applied for solid angle losses, neutron emission [20] and separation energies (based on charge distributions corresponding to these events). Here we emphasize the distinction between deposition energy, which characterizes the chaotic nucleon momentum distribution after the fast cascade, and excitation energy, which implies full statistical equilibrium. The former is more appropriate for comparison with transport models; the latter, for the disintegration of an equilibrated system. The temporal connection between these two is a complex issue, both for experiment and theory [5].

Allowing for mass loss during the fast cascade, as predicted by INC calculations [3], these deposition energies correspond to maxima of $\sim$12 MeV/nucleon and $\sim$10

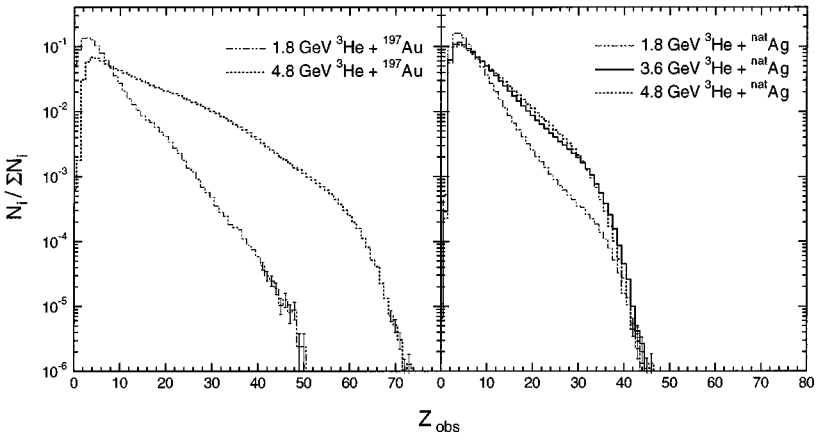

FIG. 9. Total observed charge for the 1.8 and 4.8 GeV ^{3}He+^{197}Au reactions (left) and 1.8, 3.6, and 4.8 GeV ^{3}He+^{nat}Ag reactions (right).

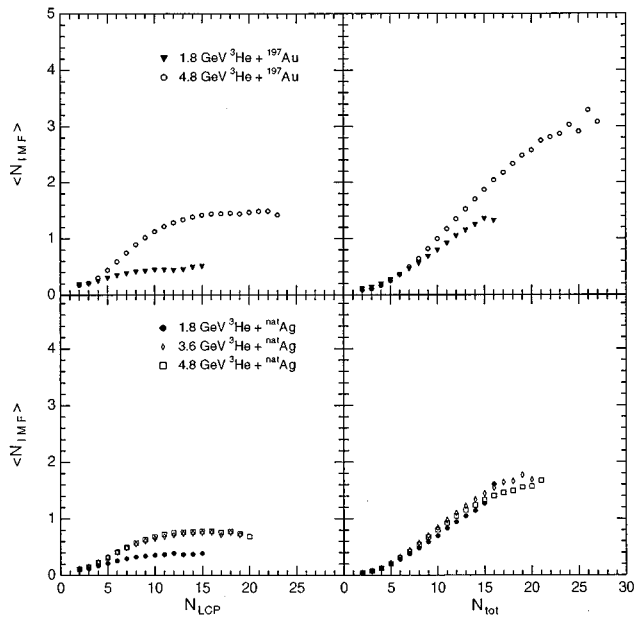

FIG. 10. The average number of observed IMF's $\langle N_{\mathrm{IMF}}\rangle$ as a function of LCP (left) and total charged-particle (right) multiplicity for ^{3}He+^{197}Au system (top) and ^{3}He+$^{\mathrm{nat}}$Ag system (bottom).

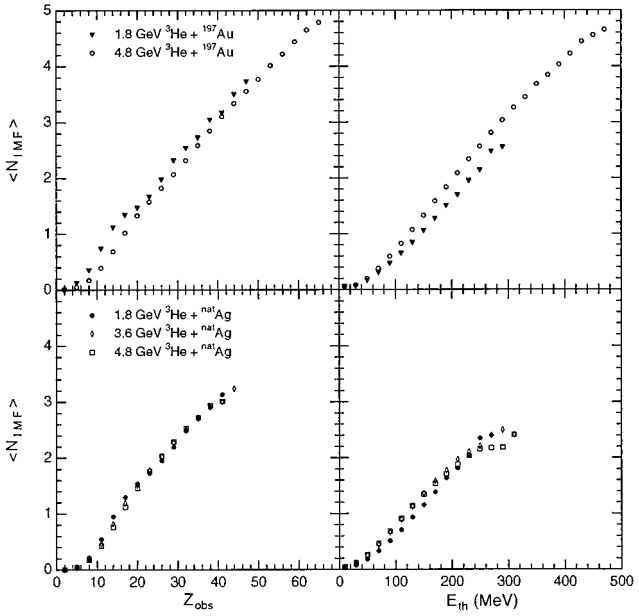

FIG. 11. $\langle N_{\mathrm{IMF}}\rangle$ as a function of total observed charge (left) and total thermalized energy (right) for ^{3}He+^{197}Au system (top) and ^{3}He+$^{\mathrm{nat}}$Ag system (right).

MeV/nucleon for the Ag and Au residues, respectively. Thus the E_{th} distributions indicate that we are observing events in which deposition energies in excess of the total nuclear binding energy are achieved. In addition, considerable thermalization must have occurred, as indicated by rapidity analyses of these systems [21,39]. However, the widths of the excitation energy distributions for a given observable (see Sec. III B) are quite broad and thus influence our estimates of the maximum deposition energies.

Another observable that provides a useful gauge of the deposition energy is the total detected charge, Z_{obs}. Since ISiS does not measure low energy recoil nuclei, Z_{obs} is directly related to the number of target plus projectile protons that participate in the reaction and subsequently appear as LCP's and IMF's. Therefore, Z_{obs} should be correlated with deposition energy. The Z_{obs} distributions are shown in Fig. 9. (The quantity Z_{obs} is the complement of Z_{bound} frequently used in inverse kinematics reactions [35]; i.e., for our system, $Z_{\mathrm{obs}}\sim Z_T - Z_{\mathrm{bound}}$.) For the Ag system, the 3.6 and 4.8 GeV ^{3}He+$^{\mathrm{nat}}$Ag results for Z_{obs} are nearly identical, further reinforcing the conclusion that deposition energy saturates near a bombarding energy of 4 GeV for the ^{3}He+$^{\mathrm{nat}}$Ag system. Otherwise, the Z_{tot} distributions scale systematically with bombarding energy and target mass. For each target, the distributions in observed charge decrease monotonically up to a value consistent with the total charge available in the reaction, corrected for detector geometric acceptance to first order ($Z\approx 33$ for Ag and $Z\approx 56$ for Au). Thereafter, the distributions decrease more rapidly, although some events are detected that contain up to 90% of the total charge.

B. Gauges of excitation energy

All models of multifragmentation [29–32,40] predict that the IMF multiplicity is correlated with excitation energy, at least up to very high excitation energies, beyond which the average IMF multiplicity begins to decrease with a corresponding increase in LCP multiplicities. The decrease at higher energy is confirmed by experimental data from heavy-ion-induced reactions [41,42]. The high excitation energies that lead to a decline in average IMF multiplicity, if accessible in light-ion-induced reactions, should be found in correlations with other observables. Under this assumption, the average IMF multiplicity, $\langle N_{\mathrm{IMF}}\rangle$, has been plotted against light-charge-particle multiplicity (N_{LCP}), total charged-particle multiplicity (N_{tot}), total observed charge (Z_{obs}), and total thermal energy (E_{th}), as shown in Figs. 10 and 11. At low N_{LCP} (the most peripheral collisions), the average observed IMF multiplicity increases monotonically. As N_{LCP} increases, the average number of IMF's emitted from the 4.8

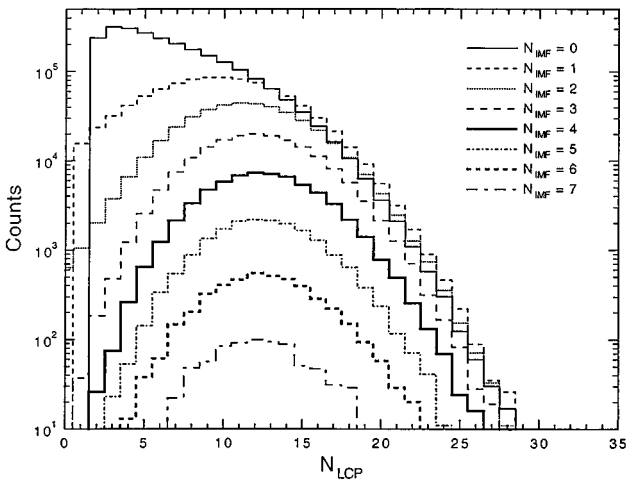

FIG. 12. LCP distributions for IMF multiplicities M_{IMF}=1–7 in the 4.8 GeV ^{3}He+^{197}Au reaction.

GeV ^{3}He+^{197}Au systems increases above those of the other systems. For all the systems, $\langle N_{\rm IMF}\rangle$ becomes nearly constant for large values of $N_{\rm LCP}$, reaching maxima near $\langle N_{\rm IMF}\rangle \approx 0.4$ for the 1.8 GeV ^{3}He+$^{\rm nat}$Ag, ^{197}Au systems, $\langle N_{\rm IMF}\rangle \approx 0.75$ for the 3.6 and 4.8 GeV ^{3}He+$^{\rm nat}$Ag systems, and $\langle N_{\rm IMF}\rangle \approx 1.5$ for the 4.8 GeV ^{3}He+^{197}Au system.

These results are consistent with INC calculations, which predict only a weak positive correlation between the fast LCP multiplicity and large deposition energies due to the very large fluctuations associated with the cascade [2,3]. This is illustrated in Fig. 12, where we show the LCP distributions as a function of IMF multiplicity for the ^{3}He+^{197}Au reaction at 4.8 GeV. Thus, the LCP multiplicity in central collisions appears to be a poor gauge of the deposition energy. This result contrasts with the conclusions of Ref. [16]; however, particle thresholds were an order of magnitude higher in that experiment.

A stronger correlation is obtained when total charged-particle multiplicity are compared with $\langle N_{\rm IMF}\rangle$; however, this may be in large part due to autocorrelation effects. All systems yield similar results for peripheral reactions, with the correlation for the 4.8 GeV ^{3}He+^{197}Au system extending to the highest IMF multiplicities. For the most dissipative collisions, the maximum $\langle N_{\rm IMF}\rangle$ reaches values approximately twice as large as for LCP's alone (i.e., maxima of $\sim$1.2 for the 1.8 GeV systems, $\sim$1.5 for the 3.6 and 4.8 GeV ^{3}He+^{197}Ag systems, and $\sim$3.0 for the 4.8 GeV ^{3}He+^{197}Au system). These results are very similar to data from comparable systems in heavy-ion-induced reactions [43–45], although heavy ions tend to yield somewhat larger maximum values of $\langle N_{\rm IMF}\rangle$ and $N_{\rm tot}$ than are observed here.

The strongest correlations with IMF multiplicities are found for total detected charge, $Z_{\rm obs}$, and the total thermalized energy, $E_{\rm th}$. For $Z_{\rm obs}$, we find that with the exception of 1.8 GeV ^{3}He+^{197}Au, all systems have nearly identical behavior over the entire observed range in $Z_{\rm obs}$, with a slope of approximately 12 charge units/IMF emitted, on average (Fig. 11). However, there is a large degree of autocorrelation between $\langle N_{\rm IMF}\rangle$ and $Z_{\rm obs}$, since higher IMF multiplicities tend to result in a higher total IMF charge and therefore higher $Z_{\rm obs}$. The deviation observed in the 1.8 GeV ^{3}He+^{197}Au system is most likely due to contributions from fission, which are most significant for this system.

The correlations for total thermalized energy are very similar to those of $Z_{\rm obs}$. Total energy and total transverse energy were also investigated. However, these yielded weaker correlations than $E_{\rm th}$, most likely due to the inclusion of a larger number of nonequilibrium particles (primarily H and He isotopes) in the calculations of the total energy and total transverse energy. Because nonequilibrium particles are emitted in the early-to-intermediate stages of the reaction, they are less valid indicators of the residue excitation energy.

One point that should be made is that $E_{\rm th}$, total energy, and total transverse energy all include contributions from the Coulomb repulsion energy of the emitted fragments and the thermal energy of the source, as well as any possible collective expansion of the system. The last of these may arise from either decompression of a system with $\rho > \rho_0$, or from thermal expansion. Since the projectile-target interaction in light-ion-induced reactions results in little density compression [5,7], thermal consequences of nucleon-nucleon collisions and pion reabsorption in the center of the nucleus should account for any radial expansion. This is discussed more fully in Ref. [21].

Based on these correlations, for light-ion-induced reactions the total observed charge and thermalized energy appear to be useful gauges of the energy dissipated by the projectile into the internal energy of the system. However, it should be stressed that in all cases, the width of the distributions is quite broad, as illustrated by Fig. 12. Thus the use of average quantities must be interpreted with some caution.

IV. INTRANUCLEAR CASCADE SIMULATIONS

In order to make meaningful comparisons between multifragmentation models and the data, it is necessary to account for the underlying collision dynamics. To achieve this, models that treat the disassembly of excited residues must be appended to some appropriate transport model to predict the mass and excitation energy distributions of the excited residues. Since there is little time for evolution of the mean field in light-ion-induced reactions, intranuclear cascade models [2,3,7] can be used to estimate energy dissipation. In contrast, for heavy-ion projectiles, the evolution of the mean field of the colliding nuclear system is significantly influenced by the reaction dynamics, and Boltzmann-Uehling-Uhlenbeck (BUU) approaches are required [8–10,46,47].

In this section, energy deposition in the ^{3}He+^{197}Ag, ^{197}Au reactions is investigated using the Weizmann Institute version of the intranuclear cascade code ISABEL [3]. The predictions of this code agree well with Refs. [2] and [7]. The intranuclear cascade results reported here were performed using the fast rearrangement options and sequential-collision exclusion within a 1.1 fm distance. These options emphasize the formation of highly excited residual nuclei—a condition necessary to enhance the probability for multifragmentation [4]. The cascade-cascade interaction serves to increase pion absorption by allowing particles that have already undergone collisions to interact further. In calculations with fast rearrangements, the volume in which an interaction takes place is instantly filled (overall density is lowered) so that additional collisions can occur in the region. This assumption has been shown to reproduce experimental data for central collisions in heavy-ion-induced reactions at similar projectile E/A values, and at the same time account for fast nucleon spectra and multiplicities [3].

ISABEL calculations were carried out for the ^{3}He+^{197}Ag, ^{197}Au systems for bombarding energies between 0.27 and 5.8 GeV. The calculation for each interaction was halted when the energy of the nucleons from each cascade fell below the energy needed to escape the nuclear well. At this point, the mass, charge, momentum vector, and excitation energy of the residual nucleus were calculated. The subsequent decay of these excited residues can then be treated in a separate calculation [4,13].

In Fig. 13, the average excitation energy of the residual nuclei predicted by the ISABEL code for the ^{3}He+$^{\rm nat}$Ag, ^{197}Au systems is shown for incident energies below 6 GeV. The curves show the average excitation energy for three impact parameter regimes: central collisions, intermediate impact parameters, and peripheral interactions. Assuming a ra-

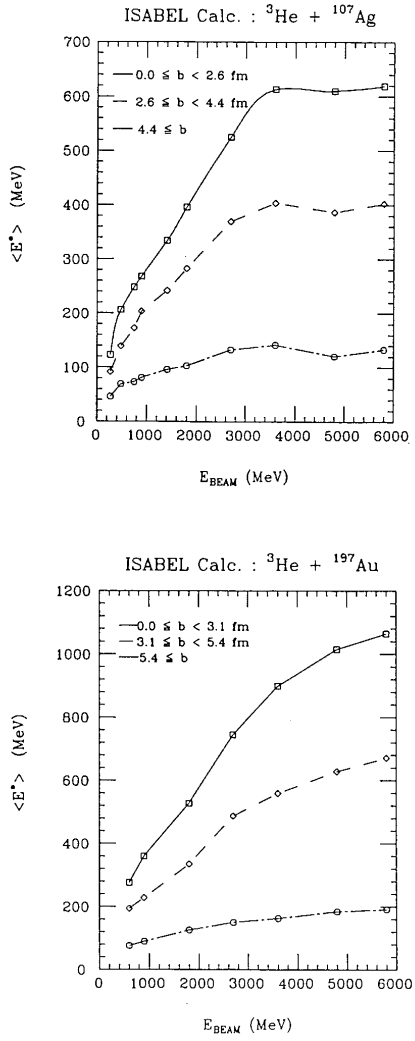

FIG. 13. Predictions of the ISABEL code (with fast rearrangement option) for average excitation energy as a function of bombarding energy for the ^{3}He+^{107}Ag, ^{197}Au systems. Results are shown for three impact-parameter regimes, as indicated in the figure.

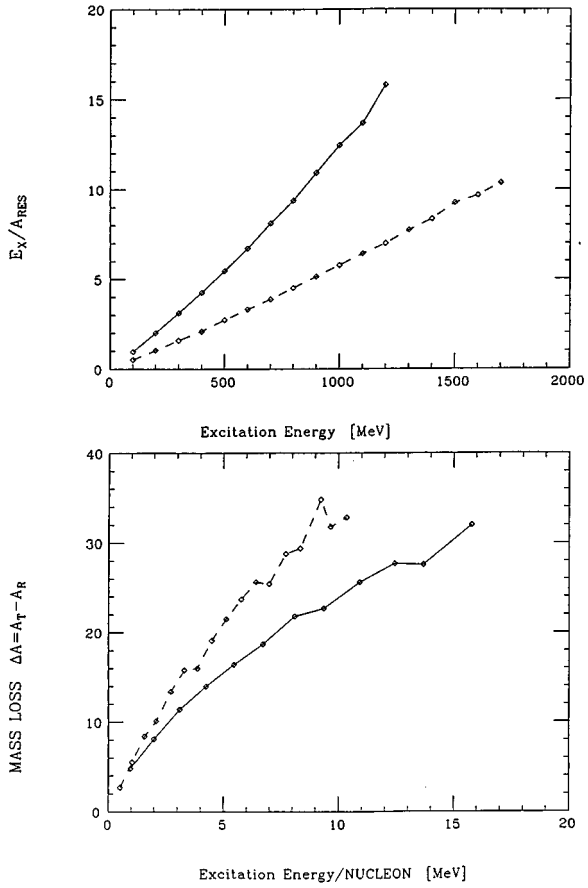

FIG. 14. Excitation energy per residue nucleon and average mass loss during the cascade (ΔA) as a function of excitation energy as predicted by the ISABEL code for the 4.8 GeV ^{3}He+^{107}Ag (solid lines), ^{197}Au (dashed lines) reactions.

dius parameter of $r_0 \simeq 1.4$ fm, these values correspond to approximately 10%, 20%, and 70% of the total reaction cross section, respectively. It is observed that for events with the largest impact parameters, i.e., most of the cross section, the average excitation energy, $\langle E^* \rangle$, remains relatively low and insensitive to bombarding energy, E_{beam}. With decreasing impact parameter, however, the average excitation energy increases much more rapidly with bombarding energy. For the ^{3}He+$^{\text{nat}}$Ag system, the code predicts a saturation in average excitation above about 4 GeV for central collisions. This behavior arises from the nucleon-nucleon scattering properties in this energy regime, as discussed in Sec. III. Also, because of the large mass loss during the initial cascade (Fig. 14), the effective density of nucleons is noticeably reduced in the later stages of the cascade [5,7].

Figure 15 shows the excitation energy distributions predicted by ISABEL for the 1.8 and 4.8 GeV ^{3}He+^{197}Au and 1.8, 3.6, and 4.8 GeV ^{3}He+^{107}Ag systems for collisions which deposit excitation energies greater than $E^* \geqslant 50$ MeV. As expected, the distributions extend to higher excitation energies for the 4.8 GeV projectiles than for 1.8 GeV. When comparing the 1.8 and 4.8 GeV results, the excitation energy distribution for ^{197}Au extends to significantly higher residue energies than for the ^{107}Ag target. One simple explanation for this is the difference in size of the two systems. The average thickness, $\langle t \rangle$, of a nucleus is given by $\langle t \rangle \approx 4/3 r_0 A^{1/3}$, $\langle t \rangle \simeq 9.3$ fm for ^{197}Au, and $\langle t \rangle \approx 7.6$ for ^{107}Ag. For a total N-N cross section of 40 mb, the average thickness for ^{197}Au is about 4.4 times greater than the nucleon mean free path, as compared to 3.7 for $^{\text{nat}}$Ag.

The qualitative correspondence between the data in Figs. 6–8 and the ISABEL calculations is good. Most significant, the INC calculations for the ^{3}He+$^{\text{nat}}$Ag system also indicate that approximate saturation in the residue deposition energy is reached at a bombarding energy near 4 GeV. This is apparent both in the excitation function of Fig. 13 and in the nearly identical probability distributions for the 3.6 and 4.8 GeV cases in Fig. 15. it should also be noted that both INC [7] and BUU [5] calculations indicate that the post-cascade residue exists in a state of depleted density (i.e., $\rho < \rho_0$). Hence the reaction dynamics may play an important role in the breakup geometry of the post-cascade residues [5,11]. Ideally, this depletion effect should be incorporated in the initial stages of theoretical treatments of the decay dynamics. As a gauge for comparison with the INC calculations, the total thermalized energy appears to be a particularly useful parameter in that it is a continuous variable, includes minimal preequilibrium contributions, and in principle, can be directly related to the residue excitation energy. However,

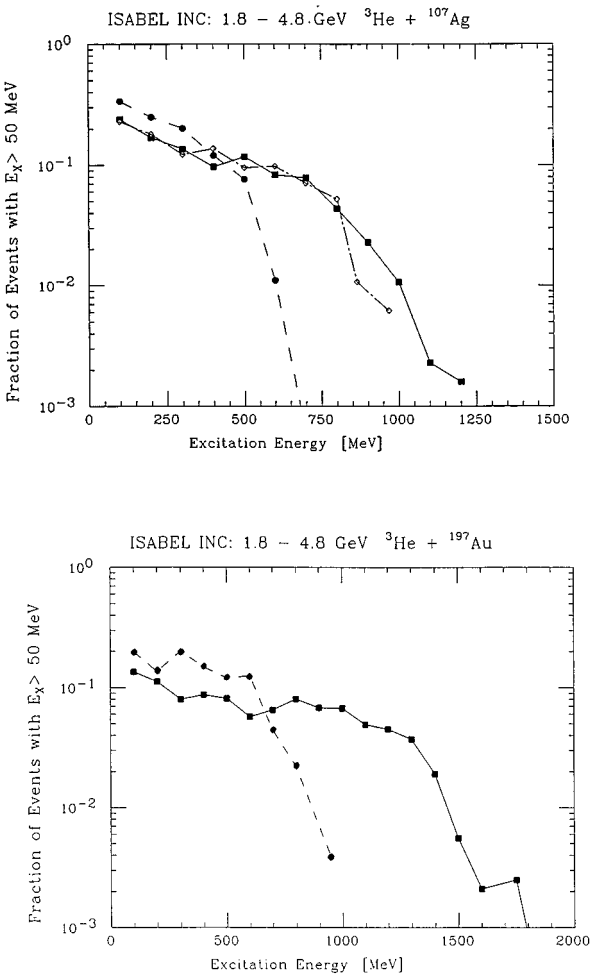

FIG. 15. Distribution of excitation energies for residues with $E^*>50$ MeV predicted by the ISABEL code for the 1.8 and 4.8 GeV ^{3}He+^{197}Au reactions (bottom) and 1.8, 3.6, and 4.8 GeV ^{3}He+^{107}Ag reactions (top). Calculations are averaged over 100 MeV bins. Symbols refer to projectile energy as follows: 1.8 GeV (circles), 3.6 GeV (diamonds), and 4.8 GeV (squares).

the direct connection between the excitation energy predictions of transport models and experimental observables is nontrivial and in this paper we only attempt to investigate the qualitative relationship.

Analysis of the INC results also sheds light on two other aspects of the data. First, the larger charged particle multiplicities for the ^{3}He+^{nat}Ag system at 4.8 GeV relative to 3.6 GeV (Figs. 4 and 6), were ascribed to fast particle emission. The INC calculations support this interpretation, predicting more fast cascade particles at 4.8 GeV than at 3.6 GeV, despite nearly identical excitation energy distributions. Second, the maximum excitation energies predicted by the INC code at 4.8 GeV are of the order of 1.0 GeV for the ^{nat}Ag target and 1.5 GeV for ^{197}Au. These values roughly correspond to those inferred from the maximum measured E_{th} results in Fig. 8. Although the fraction of events with $E^*\geqslant 500$ MeV is much higher for the ^{197}Au target (Fig. 15), the excitation energy per residual nucleon, $\langle E^*/A\rangle$, extends to larger values for ^{107}Ag, as shown in Fig. 14. The maximum values correspond to $E^*/A\approx 13$ MeV per residue nucleon for the Ag target and $E^*/A\approx 9$ MeV/residue nucleon for ^{197}Au.

V. CONCLUSIONS

In summary, we have investigated the collision dynamics in GeV light-ion-induced reactions by measuring LCP's and IMF's with a low-threshold 4π charged-particle detector array. Several experimental observables related to the projectile energy dissipation and excitation deposited in the target-like residue have been examined. In addition, on the basis of the systematics of the fragment LCP and IMF spectra, we have separated the distributions into thermal and fast components.

In terms of deposition energy—most relevant to defining the thermal properties of the residues—it is argued that the most valid experimental signatures are found in the IMF and total-thermal-LCP multiplicities, the total observed charge, and the total thermalized energy. Correlations of these observables with the average IMF multiplicity reinforce this conclusion. We also show that the total thermal energy distribution scales with that for total transverse energy; however, the total transverse energy is also sensitive to nonequilibrium events. The LCP and total-charged-particle multiplicities, as well as the total observed energy per event, are shown to contain significant fast-cascade/nonequilibrium components. Thus they relate more to the energy dissipation by the projectile than to the excitation energy deposited in the residue. The presence of significant nonequilibrium emission in these data emphasizes the importance of eliminating such events in any attempt to evaluate the residue excitation energy.

For all distributions, the maximum value of a given observable increases as a function of increasing projectile energy for each target and as a fraction of projectile mass for a fixed bombarding energy. The exception is the ^{3}He+^{nat}Ag system, where the results show a saturation in deposition energy near 4 GeV. This is consistent with the observation of limiting fragmentation and constant charge distributions for light-ion-induced reactions in this energy region [14]. From the thermal energy distributions and the associated fragment charge distributions, we estimate the most violent events produce deposition energies up to $E^*\sim 950$ MeV for ^{nat}Ag and $E^*\sim 1600$ MeV for ^{197}Au. The values correspond to maximum values of $E^*A\sim 12$ MeV for the Ag-like residue and $E^*/A\sim 10$ MeV for the Au-like residue—indicating that the total LCP vaporization regime should be accessible in GeV light-ion-induced reactions.

Finally, comparison of the experimental results with the intranuclear cascade code ISABEL shows good qualitative correspondence. In particular, the code predicts the observed saturation in deposition energy for the ^{3}He+^{nat}Ag system near 4 GeV bombarding energy. Also, the predicted relative cross section for excitation energies that exceed the multifragmentation threshold ($\sim$500 MeV) appear to be consistent with the cross section values determined in Ref. [21]. Thus, the INC model appears to provide a reasonable basis for describing the collision dynamics in GeV light-ion reactions. However, a quantitative relationship between the experimental observables and transport code predictions of the deposition energy remains an important future objective.

ACKNOWLEDGMENTS

We thank the technical staff of DAPNIA/CE Saclay, as well as J. Arvieux and the staff at LNS for their support in

making these experiments possible; in particular, G. Milleret for his assistance with the beam tuning optics. Among the numerous individuals who contributed to the success of this project were F. Haroutel, A. Mansion, J. Faure, J. C. Lugol, and his staff, W. Lozowski, J. P. Passerieux, C. Mazur, K. McDonald, T. Hamilton, C. Powell, J. Dorsett, A. Alexander, J. Poehlman, and K. Komisarcik. We also thank Z. Fraenkel for providing the ISABEL code to us and W. Bauer and P. Danielewicz for fruitful discussions of the reaction dynamics. The authors acknowledge the primary financial support of the U.S. Department of Energy; additional support was provided by Indiana University, Commissariat à l'Energie Atomique (France), the U.S. National Science Foundation, the National Science and Energy Research Council (Canada), NATO, and KBN Grant No. 0719/P3/93/04 (Poland).

[1] R. Wolfgang, E. W. Baker, A. A. Caretto, J. B. Cumming, G. Friedlander, and J. Hudis, Phys. Rev. **103**, 394 (1956).
[2] J. Cugnon, D. Kinet, and J. Vandermuelen, Nucl. Phys. **A379**, 553 (1982); **A462**, 751 (1987).
[3] Y. Yariv and Z. Fraenkel, Phys. Rev. C **24**, 488 (1981); **20**, 2227 (1979).
[4] K. Kwiatkowski, W. A. Friedman, L. W. Woo, V. E. Viola, E. C. Pollacco, C. Volant, and S. J. Yennello, Phys. Rev. C **49**, 1516 (1994).
[5] G. Wang, K. Kwiatkowski, V. E. Viola, W. Bauer, and P. Danielewicz, Phys. Rev. C **53**, 1811 (1996).
[6] A. Y. Abdul-Magd, W. A. Friedman, and J. Hüfner, Phys. Rev. C **34**, 113 (1986).
[7] V. S. Barashenkov, A. S. Iljinov, and V. D. Toneev, Sov. J. Nucl. Phys. **13**, 422 (1971); Acta Phys. Pol. B **1**, 219 (1973); E. S. Golubeva *et al.*, Phys. At. Nucl. **57**, 2084 (1994).
[8] G. F Bertsch, H. Kruse, and S. Das Gupta, Phys. Rev. C **29**, 673 (1984).
[9] P. Danielewicz and G. F. Bertsch, Nucl. Phys. **A533**, 712 (1991); P. Danielewicz (private communication).
[10] W. Bauer, G. F. Bertsch, W. Cassing, and U. Mosel, Phys. Rev. C **34**, 2127 (1986); B.-A. Li, W. Bauer, and G. F. Bertsch, *ibid.* **44**, 2095 (1991).
[11] S. Pratt, Phys. Rev. A **42**, 1447 (1990); S. Pratt *et al.*, Phys. Lett. B **349**, 251 (1995).
[12] H. Müller and B. D. Serot, Phys. Rev. C **52**, 2072 (1995).
[13] J. Cugnon and C. Volant, Z. Phys. A **334**, 435 (1989).
[14] W. G. Lynch, Annu. Rev. Nucl. Sci. **37**, 493 (1987).
[15] K. Nakai, Nucl. Phys. **A379**, 553 (1982); **A462**, 751 (1987).
[16] A. I. Warwick, H. H. Wieman, H. H. Gutbrod, M. R. Maier, J. Péter, H. Stelzer, and F. Welk, Phys. Rev. C **27**, 1083 (1983).
[17] F. Saint Laurent, M. Conjeaud, R. Dayras, S. Harar, H. Oeschler, and C. Volant, Nucl. Phys. **A422**, 307 (1984).
[18] M. Fatyga, K. Kwiatkowski, H. J. Karwowski, L. W. Woo, and V. E. Viola, Phys. Rev. C **32**, 1496 (1985); L. W. Woo, K. Kwiatkowski, and V. E. Viola, Phys. Lett. **132B**, 283 (1993).
[19] G. Klotz-Engmann *et al.*, Nucl. Phys. **A499**, 392 (1989).
[20] L. Pienkowski *et al.*, Phys. Lett. B **336**, 147 (1994).
[21] E. Renshaw Foxford *et al.*, following paper, Phys. Rev. C **54**, 749 (1996).
[22] K. B. Morley *et al.*, Phys. Lett. B **355**, 52 (1995).
[23] K. Kwiatkowski *et al.*, Phys. Rev. Lett. **74**, 3756 (1995).
[24] K. Kwiatkowski *et al.*, Nucl. Instrum. Methods A **360**, 571 (1995).
[25] W. Lozowski, Indiana University Cyclotron Facility.
[26] J. P. Passerieux, CEN Saclay report (1993).
[27] D. Powers, W. K. Chu, R. J. Robinson, and A. S. Lodhi, Phys. Rev. A **6**, 1425 (1972).
[28] DONNA code, W. G. Meyer (unpublished).
[29] L. G. Moretto and G. J. Wozniak, Annu. Rev. Nucl. Part. Sci. **43**, 371 (1993).
[30] W. A. Friedman, Phys. Rev. C **42**, 667 (1990).
[31] J. P. Bondorf, R. Donangelo, I. N. Mishustin, C. J. Pethick, H. Schulz, and K. Sneppen, Nucl. Phys. **A443**, 321 (1985).
[32] D. H. E. Gross, Rep. Prog. Phys. **53**, 605 (1990).
[33] V. Lips *et al.*, Phys. Rev. Lett. **72**, 1604 (1994).
[34] D. R. Bowman *et al.*, Phys. Rev. Lett. **67**, 1527 (1991).
[35] W. Trautman, in *Towards a Unified Picture of Nuclear Dynamics*, AIP Conf. Proc. No. 250, edited by F. Sakata (AIP, New York, 1991), p. 409.
[36] D. S. Bracken, Ph.D. thesis, Indiana University, 1996.
[37] G. Westfall, *et al.*, Phys. Rev. C **17**, 1318 (1978).
[38] G. Bertsch, in *Nuclear Physics with Heavy Ions and Mesons*, edited by R. Balian, M. Rho, and G. Ripka (North-Holland, Amsterdam, 1978), Vol. 1, p. 251.
[39] S. J. Yennello *et al.*, Phys. Rev. C **48**, 1092 (1993).
[40] J. Randrup and S. Koonin, Nucl. Phys. **A356**, 223 (1981); J. A. Lopez and J. Randrup, *ibid.* **A491**, 477 (1989).
[41] J. Hubele *et al.*, Z. Phys. A **340**, 263 (1991).
[42] G. F. Peaslee *et al.*, Phys. Rev. C **49**, R2271 (1994).
[43] D. R. Bowman *et al.*, Phys. Rev. C **46**, 1834 (1992).
[44] L. Phair *et al.*, Phys. Lett. B **285**, 10 (1992).
[45] F. Saint-Laurent *et al.*, Nucl. Phys. **A583**, 481 (1995).
[46] H. Kruse, B. V. Jacak, J. J. Molitoris, G. D. Westfall, and H. Stöcker, Phys. Rev. C **31**, 1770 (1985).
[47] J. Aichelin, Phys. Rep. **202**, 233 (1991).